Research Article | Vol. 31, No. 21 / 9 Oct 2023 / Optics Express 34697
Optics EXPRESS

Substrate-embedded metal meshes for ITO-free organic light emitting diodes

MEHDI ZAREI,[1] JAMES C. LOY,[2] MINGXUAN LI,[3] ZIYU ZHOU,[1] SNEH SINHA,[4] MELBS LEMIEUX,[4] S. BRETT WALKER,[4] BARRY P. RAND,[5,6] AND PAUL W. LEU[1,3,7,*]

[1]*Department of Mechanical Engineering and Material Sciences, University of Pittsburgh, Pittsburgh, PA 15261, USA*
[2]*Department of Physics, Princeton University, Princeton, NJ 08544, USA*
[3]*Department of Chemical Engineering, University of Pittsburgh, Pittsburgh, PA 15261, USA*
[4]*Electroninks Incorporated, 7901 East Riverside Drive, Bldg. 1, Unit 150, Austin, TX 78744, USA*
[5]*Department of Electrical and Computer Engineering, Princeton University, Princeton, NJ 08544, USA*
[6]*Andlinger Center for Energy and the Environment, Princeton University, Princeton, NJ 08544, USA*
[7]*Department of Industrial Engineering, University of Pittsburgh, Pittsburgh, PA 15261, USA*
[*]*pleu@pitt.edu*

Abstract: Organic light-emitting diodes (OLEDs) have great potential for use in large-area display and lighting applications, but their widespread adoption for large areas is hindered by the high cost and insufficient performance of indium tin oxide (ITO) anodes. In this study, we introduce an alternative anode material – a silver mesh embedded in glass – to facilitate production of large-area OLEDs. We present a facile, scalable manufacturing technique to create high aspect ratio micromeshes embedded in glass to provide the planar geometry needed for OLED layers. Our phosphorescent green OLEDs achieve a current efficiency of 51.4 cd/A at 1000 cd/m^2 and reach a slightly higher external quantum efficiency compared to a standard ITO/glass reference sample. Notably, these advancements are achieved without any impact on the viewing angle of the OLEDs. These findings represent a promising advancement towards ITO-free, high-efficiency OLEDs for various high performance, large-area applications, such as lighting and displays.

1. Introduction

Organic light-emitting diodes (OLEDs) have been the focus of significant research and development efforts which have resulted in commercial success in the mobile device, television, and wearables sectors. They boast a range of key characteristics including high contrast ratio, wide viewing angle, fast switching speed, and high luminous efficiency [1–7]. Additionally, their low power consumption, eco-friendly materials, and uniform illumination make them ideal for large area lighting applications.

Indium tin oxide (ITO) is commonly used as the transparent conducting electrode in OLEDs, but it has several economic and technological limitations. Indium is a scarce element, making its incorporation into large area electronics expensive. The deposition of ITO typically involves physical vapor deposition (PVD), a process requiring high energy consumption, high vacuum, and high capital investment. Additionally, the brittleness of ITO renders it impractical for flexible substrates, limiting its use in flexible or bendable applications [8]. With regard to optical and electronic properties, 150 nm thick ITO can typically achieve a transparency and sheet resistance R_s in the range of 85-92% and 50-100 Ω/sq, respectively. This performance is inadequate for large area optoelectronic applications without integrating metal meshes [9]. Furthermore, the high refractive index of ITO ($n \approx 1.8 - 2$ in the visible light range) results in considerable waveguiding losses and thereby limiting the fraction of outcoupled light [8,10].

#499932 https://doi.org/10.1364/OE.499932
Journal © 2023 Received 6 Jul 2023; revised 31 Aug 2023; accepted 1 Sep 2023; published 2 Oct 2023

Optics EXPRESS

As a result, there has been growing interest in exploring ITO alternatives, which may offer advantages such as mechanical flexibility and compatibility with roll-to-roll manufacturing processes. These materials include conducting polymer thin films [11,12], carbon-based nanomaterials (such as carbon nanotubes [13] and graphene [14,15]), and metal-based materials [16–21]. Poly(3,4-ethylenedioxythiophene) (PEDOT:PSS)(n = 1.5) is a commonly used conducting polymer that is relatively low cost compared to other transparent electrode materials [11]. However, it faces limitations for optoelectronic applications such as low conductivity, poor durability when exposed to high temperature, humidity, or UV light, and a non-neutral-color which influences the emission spectrum to some extent [22]. While individual carbon nanotubes and graphene exhibit excellent conductivity, their thin film composites have multiple junctions or grain boundaries, leading to high resistivity [2,3].

Metal-based electrodes, such as ultrathin metal films [23,24], metal nanowire networks [25–32], and metal meshes [17,18,33–40] have also been the source of much research interest. These materials offer high conductivity, adjustable transmittance, and adaptable flexibility, which make them a promising candidate for transparent electrodes. Ultrathin metal films rely on PVD techniques such as thermal evaporation or sputtering to produce smooth and consistently thin coatings. However, similar to ITO, these PVD techniques are expensive due to the requirement of high vacuum and costly equipment. Ultrathin films tend to have wettability issues on various substrates, which may require a seeding layer or doping to ensure uniformity [3], and there are fundamental tradeoffs where very thin films have high sheet resistance and thick films have low transparency. Metal nanowires, such as silver and copper nanowires, also have issues with contact resistance at the wire-to-wire junctions [25–29,41].

Metal meshes offer an alternative to metal nanowires, avoiding the challenges with contact resistance at wire junctions. Adjusting the sheet resistance and optical transmittance is possible by modifying parameters like the linewidth, thickness, pitch, and pattern shape [33,34,42]. Metal meshes may also be integrated with other nanomaterials such as metal nanowires [28], graphene [37], and metal nanomeshes [38] to improve performance at the expense of more complicated fabrication processes.

Several research studies have demonstrated the potential of using various metal electrodes and device structures in creating OLEDs [17,18,28,35,43–48]. Previous research on metal mesh-based OLEDs involved printed or sputtered metal meshes [35,48]. However, metal meshes have drawbacks such as poor adhesion to PEDOT:PSS and the potential for short-circuiting due to protruding structures.

In a study by Sam *et al.* [35], silver hexagonal meshes were created on a glass substrate using photolithography. However, the thickness of the silver meshes could not exceed 100 nm, which resulted in high R_s= 10 Ω/sq. A printed Cu mesh on a glass substrate, even with a maximum thickness of 136 nm only achieved an R_s of 13 Ω/sq and a transmittance of 80%. In a recent study by Wang *et al.* [49], a random metallic mesh was fabricated on PET via a crack-template lift-off process. A 100 nm thick metallic mesh with R_s= 10.6 Ω/sq and transmittance of 80.6% was demonstrated. The thickness of metal layers has been limited by the deposition and printing methods used thus far. Printing methods such as inkjet, gravure, screen, and spin coating lead to thick metal layers where the abrupt changes in geometry may cause shorting in the OLED layers.

Although using embedded metal mesh structures is a possible solution to these issues, this approach has not been extensively studied [17,18]. Zhou *et al.* [18] were the first to fabricate an embedded silver mesh within a flexible substrate. Hexagonal Ag patterns with a thickness of 2 μm were fabricated and achieved R_s= 5 Ω/sq and T = 87%. The fabrication process was complicated and involved the use of electroforming to create a Ni mold. To address these issues, ink-based metal deposition methods have been reported as an effective approach to fabricate metal films on various surfaces [50–52]. However, embedded metal meshes in glass substrates have not been studied.

Optics EXPRESS

In this work, we present the fabrication of a phosphorescent green OLED on a glass-embedded Ag micromesh using a combination of lithography and reactive ion etching (RIE) processes. The trenches were filled with a highly conductive reactive silver ink that utilizes low-temperature curing (below 110 °C). The process is compatible with cost-efficient and scalable roll-to-roll manufacturing. We demonstrate a phosphorescent green OLED with a current efficiency of 51.4 cd/A at 1000 cd/m^2 and with slightly higher external quantum efficiency (EQE) compared to the ITO/glass reference device.

2. Results and discussion

Our approach to fabricating large area Ag micromeshes with narrow width and large thickness is schematically shown in Fig. 1. These micromeshes are directly embedded into glass to demonstrate their potential as transparent OLED electrodes. Initially, a glass substrate (a) is coated with photoresist (b), and a hexagonal pattern is created on it through maskless photolithography (c). The pattern is then transferred to the glass substrate using RIE (d). Afterward, the photoresist is stripped (e). Next, Ag ink is applied onto the glass by spin coating and cured (f). Subsequently, Ag is scraped off using a blade (g) to expose the final structure (h). Finally, PEDOT:PSS is spin coated on the glass-embedded Ag micromesh (i).

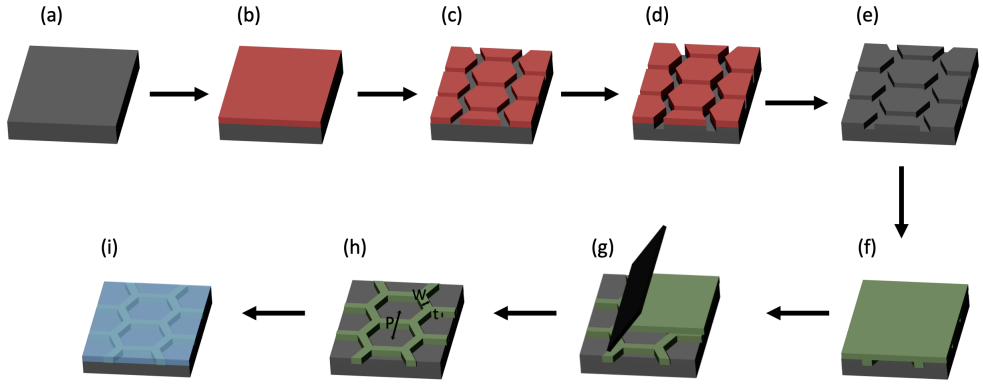

Fig. 1. Fabrication process flow for the glass-embedded Ag micromesh: (a) transparent glass substrate, (b) photoresist coating, (c) photolithography, (d) reactive-ion etching, (e) photoresist stripping, (f) Ag ink coating and curing, (g) removal of excess silver with a blade, (h) glass-embedded Ag mesh, and (i) PEDOT:PSS coating. The Ag micromesh, illustrated in (h), is a hexagonal array defined by width W, pitch P, and thickness t.

Figure 2 provides a visual characterization of the sample at various stages of fabircation. In Fig. 2(a), the glass sample is shown before silver coating, while in Fig. 2(b) and (c), it is shown after the silver and PEDOT:PSS coating. Figure 2(a) shows a 2D color map image of the fabricated sample where uniform trenches with a nominal width and pitch of 1 and 25 μm, respectively, were created. Additionally, the profile scanlines are shown across the $x-$ and $y-$ directions, indicating a uniform depth of 0.8 μm achieved through a 700 s RIE process. The metal mesh is defined by the mesh width W, pitch P, and thickness t.

The choice of parameters for the Ag micromesh, including W, P, and t, was guided by several considerations. The minimum feasible width achievable through maskless lithography is 1 μm, which is optimal for ensuring successful fabrication. This width facilitates the effective filling of trenches with silver ink, thus enhancing overall performance. Additionally, this width diminishes the risk of shorting incidents across the samples. A P of 25 μm was selected to strike a balance between high transmission and low sheet resistance. This choice is informed by our previous research [51], which indicates that this P yields satisfactory results for both criteria. During the

Optics EXPRESS

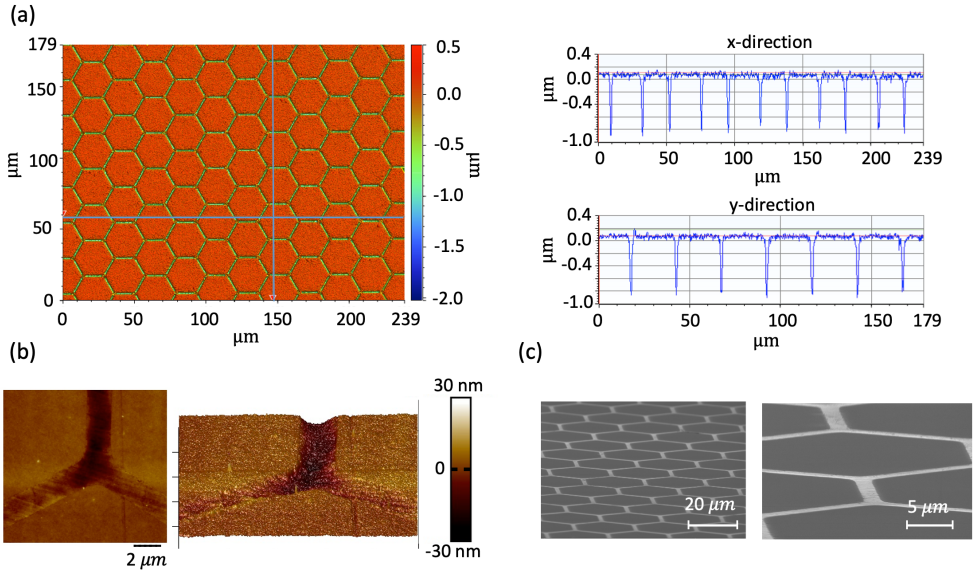

Fig. 2. Surface characterization of Ag micromesh coated with 70 nm PEDOT:PSS. (a) Op2cal profilometry analysis of glass before silver coating, showing a 2D color map image and topography profiles in both x- and y-directions. (b) AFM characterization with 2D and 3D views. (c) SEM images captured at an 80° angle from overhead, presented at different magnifications.

etching process, both the photoresist and glass undergo etching. However, it is essential to cease etching after the removal of the photoresist to avoid introducing defects in the glass substrate.

Figure 2(b) presents the atomic force microscopy (AFM) characterization of the electrodes after both silver and PEDOT:PSS coating in 2D and 3D views. It is evident from the images that the surface is smooth with a low mean square roughness R_q of 2.5 nm. Scanning electron microscope (SEM) images were also obtained, and the results are shown in Fig. 2(c). The SEM images were captured at 80° from overhead at different magnifications. The SEM images confirm the even distribution of silver filling in the trenches and the absence of silver traces between the trenches, leading to high transmission.

Figure 3 presents the optical properties of the glass and two transparent electrodes, ITO on glass and Ag micromesh coated with 70 nm PEDOT:PSS on glass. Figure 3(a) displays the transmission vs. wavelength in the visible range of 400 - 800 nm. In contrast to ITO, which exhibits significant variation across the visible wavelength range, the Ag micromesh maintains a consistent level of transmission. The transmission and conductivity of the Ag micromesh can be tuned by altering its width, pitch, and thickness [18,33]. The Ag micromesh shown here has a nominal width of 1 μm, pitch of 25 μm, and thickness of 0.8 μm. Its visible transmission is approximately 84% after being coated with PEDOT:PSS and excluding the glass substrate's contribution. Its visible transmission is approximately 84%, as determined after the application of the PEDOT:PSS coating. To account for substrate effect, we divided the measured transmission by the transmission of the glass substrate. The micromesh coated with 70 nm PEDOT:PSS has a sheet resistance of R_s = 1.1 Ω/sq, which is comparable to the best transparent conductive electrodes [2,18,33].

The Ag mesh has a period that is several orders of magnitude larger than the visible wavelength resulting in reduced light diffraction. One of the key aspects in display applications is the transmittance haze, which measures the ratio of light that is scattered to the overall amount of

Optics EXPRESS

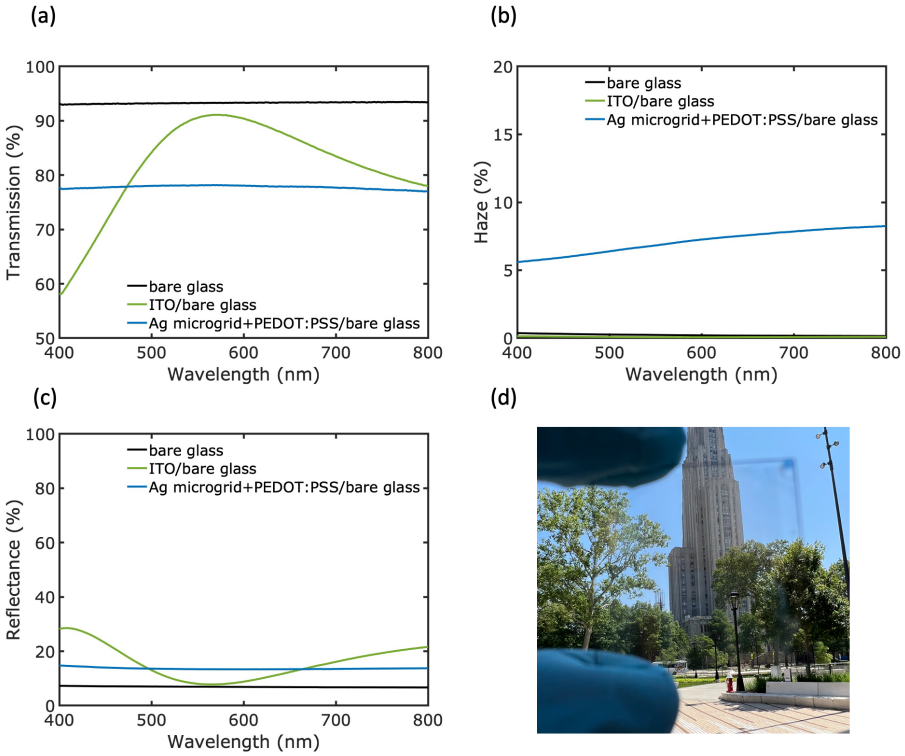

Fig. 3. Optical characteristics of glass-embedded Ag micromesh and PEDOT:PSS compared to ITO. (a) Transmission versus wavelength, (b) haze versus wavelength (c) reflectance versus wavelength, and (d) optical image of a 3 x 3 cm sample of glass-embedded Ag micromesh and PEDOT:PSS with T = 78% at 550 nm.

light transmitted [53]. Figure 3(b) depicts the haze as a function of wavelength. The ITO-coated glass exhibits an average haze of 0.9% within the visible wavelength range. In contrast, the Ag micromesh demonstrates a significantly higher average haze of 7.1% for the same wavelength range. Increased levels of haze can be advantageous for OLED efficiency as they help suppress internal waveguide modes that occur at the electrode-OLED layer interface. Hexagonal patterns applied to the glass surface effectively enhance haze, which is desirable for achieving higher EQE. Additional scattering structures may further increase haze [53–55] and improve EQE. Figure 3(c) plots the reflectance vs. wavelength. Bare glass and Ag micromeshes have nearly constant reflectance with an average of 6.9 and 13.6%, respectively. The optical image of a 3 x 3 cm Ag micromesh coated with 70 nm PEDOT:PSS is presented in Fig. 3(d).

The schematic of the OLED stack fabricated on glass-embedded Ag micromesh can be seen in Fig. 4(a). On top of the Ag micromesh, a 70 nm coating of PEDOT:PSS was applied. Unlike ITO, which covers the entire pixel, the Ag micromesh only covers a small portion of the pixel, leaving the rest of the surface as bare glass.

Consequently, to enhance lateral charge transport in the interstices of the mesh and to maximize charge injection into the whole device area, the presence of a laterally conductive layer like PEDOT:PSS is essential. The PEDOT:PSS further helps to planarize the top surface for the deposition of the various OLED layers. Because the various OLED layers are very thin, they must be deposited on a surface with minimal roughness to reduce short circuit leakage. As discussed above, the mean square roughness of the top surface is 2.5 nm.

Optics EXPRESS

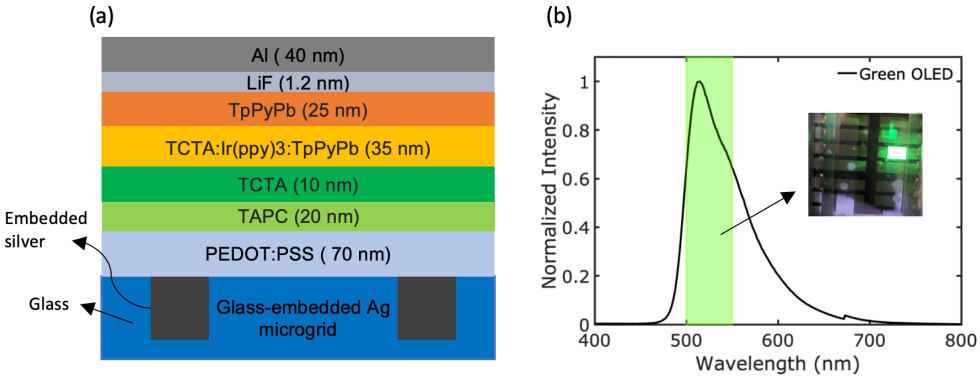

Fig. 4. OLED structure and emission properties. (a) Schematic of stacked green OLED on top of glass-embedded Ag micromesh. (b) Normalized intensity vs. visible wavelength for green OLED. Inset: Optical image of green Ag micromesh in operation.

The hole-transporting layer consists of 20 nm of 1,1-bis[(di-4-tolylamino)phenyl]cyclohexane (TAPC) followed by 10 nm of 4,4',4"-tris(carbazol-9-yl)triphenylamine (TCTA). For the emissive layer, a 35 nm thick mixture of equal parts TCTA and 1,3,5-tri(p-pyrid-3-yl-phenyl)benzene (TpPyPB) was doped with the green triplet emitter tris(2-phenylpyridine)iridium(III) ($Ir(ppy)_3$). The electron-transport layer was formed by 25 nm of TpPyPB, terminating with a bilayer LiF and Al cathode (1.2 nm and 40 nm respectively).

The emission spectrum of the devices is shown in Fig. 4(b), and shows a dominant emission in the green wavelength range with peak emission at 515 nm. The peak wavelength does not align with the maximum transmission of ITO/bare glass, as seen in Fig. 3(a). In contrast, the Ag micromesh's transmission shows no significant wavelength dependence over the OLED's en2re emission spectrum. The inset of Fig. 4(b) shows an operating OLED, demonstrating uniform emission over the 0.1 cm^2 active area.

Figure 5 shows the OLED performance of the devices with the two types of transparent electrodes. The current density-voltage plot in Fig. 5(a) demonstrates the similarity of the devices, allowing us to reasonably compare their performances. Both devices demonstrate very low leakage current before turn-on, indicative of success in achieving a planarized surface through the combination of scraping, cleaning, and coating the substrates with PEDOT:PSS. The turn-on voltage is the threshold voltage at which the OLED device initiates light emission and conducts current significantly. It marks the juncture where the current begins to rise sharply. In the case of both devices, the turn-on voltage occurs at about 2.5 V, which aligns with the typical behavior observed for green emitters. The turn-on voltage for both devices occur at 2.5 V as is typical for green emitters. The ITO control achieves a much higher current density of 100 mA/cm^2 at 5 V, compared to the micromesh's 10 mA/cm^2 at the same voltage. We attribute this discrepancy to the planar ITO having a much larger surface area to conduct current into the PEDOT:PSS layer, while the micromesh has necessarily less area to accomplish the same. The conductivity of the PEDOT:PSS was adjusted using various commercially available grades to enhance current injection in the micromesh device, emphasizing the importance of achieving a balance. At lower conductivities, the current densities are subdued compared to the ITO control for a specific voltage. However, at higher conductivities, device performance is predominantly affected by current leakage within the PEDOT:PSS layer-plane, complicating accurate area determination and efficiency measurements. Ideally, the PEDOT:PSS layer's conductivity should be adjusted to be low enough to prevent device shorting, yet remain high enough to facilitate lateral current injection within the active area, charging the hexagonal glass regions surrounded by the anode

Optics EXPRESS

mesh. Achieving this balance is very difficult in practice and beyond the scope of the present work, but offers a promising future direction to pursue.

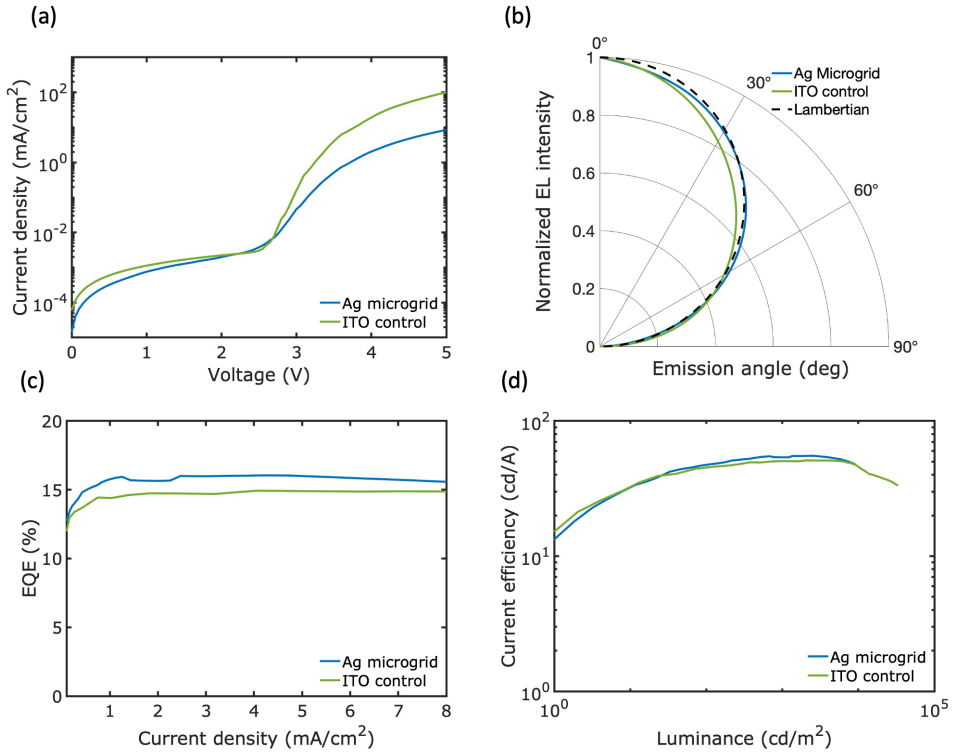

Fig. 5. Performance evaluation of glass-embedded Ag micromesh green OLED compared to the ITO/glass control sample: (a) normalized EL intensity vs. emission angle; (b) current density vs. voltage; (c) EQE vs. current density; and (d) current efficiency vs. luminance.

Both devices have nearly identical angular emission profiles (Fig. 5(b)), andclosely follow a Lambertian profile. Closer inspection reveals that the emission profile of the micromesh follows the Lambertian profile even more closely than the control sample, which is indicative of some loss mechanism for light in the emission range of 15-60°. This is consistent with ITO waveguide-trapping due to its high index of refraction and relatively high layer thickness. By removing this layer we are able to restore a more Lambertian profile to our OLEDs and emit more photons otherwise trapped in the ITO layer. This is how the Ag micromesh has similar EQE to the control ITO device despite evidence of relative current injection issues when comparing $J - V$ characteristics. Although the $J - V$ characteristics of the micromesh samples can be improved through doping, the optical losses due to waveguide trapping in the ITO device are not as easily addressed. This indicates a strength of the micromesh samples that could be leveraged to consistently outperform standard ITO architectures.

In regions where the devices have comparable current densities, the micromesh sample's EQE performance is on par with, if not slightly better than, the ITO control (Fig. 5(c)). Both devices show very stable EQE over the range of current densities with negligible rolloff. Even though the silver micromesh has a lower transmittance for green light emission (500 - 550 nm wavelength), it achieves a higher EQE than the ITO /glass controls sample. This is because the silver micromesh has a much lower sheet resistance R_s= 1.1 Ω/sq, compared to the ITO/glass control sample, which has R_s= 78.2 Ω/sq. Figure 5(d) shows that both devices are comparable in their current efficiency over the range of luminance that the micromesh samples achieve, with a slight edge to

Optics EXPRESS

the micromesh over the measured range. Ag micromesh and ITO/glass control devices achieve current efficiencies of 51.4 and 49.1 cd/A at a luminance of 1000 cd/m^2, respectively.

3. Conclusion

In conclusion, this study presents a promising solution to the challenges faced by OLED technology in wearable electronics, displays, and lighting applications. By introducing an embedded silver mesh on glass that can replace ITO, the production of large-area green OLEDs becomes feasible. The manufacturing technique proposed in this paper is to both straighxorward to implement and scalable, involving the use of reactive particle-free silver ink to fill the trenches, instead of costly methods like sputtering or thermal evaporation. The phosphorescent green OLED achieved a current efficiency of 51.4 cd/A at a luminance of 1000 cd/m^2, EQE slightly surpassing that of the ITO/glass reference sample. These findings mark a significant step forward towards realizing high-efficiency OLEDs that are ITO-free and can be utilized in diverse high-performance lighting applications.

4. Experimental

4.1. Ink information

This study utilized EI-1207, a silver metal-complex based conductive ink from Electroninks Inc, which is commercially available. The ink has a viscosity of 8 cps and a solid content of around 12 %. The ammonia ligands compounds in the ink serve as a stabilizer and evaporate during the curing process by heating, leading to the reduction of the silver compound and the formation of silver. The ink was previously developed by one of the authors [56].

4.2. Fabrication of silver mesh glass

Figure 1 illustrates the process for fabricating glass-embedded Ag micromesh. A fused silica glass substrate of size 30 mm x 30 mm was purchased from UniversityWafers and cleaned ultrasonically with acetone, methanol, and isopropyl alcohol 10 minutes each, followed by drying with nitrogen. To enhance photoresist adhesion, the substrate underwent HMDS treatment using a vapor prime oven system. S1805 photoresist was spin-coated onto the substrate at 1500 rpm, resulting in a thickness of 0.6 μm, and then baked at 110 °C for 5 minutes. Patterns were created on the photoresist using Heidelberg MLA100 Direct Write Lithography and developed in AZ400 K (1:4) from MicroChemicals for 2 minutes. The patterns were transferred onto the glass substrate using a reactive-ion etching (RIE) process with a gas flow of 50 sccm Ar and 25 sccm CHF3, a pressure of 30 mT, and a power of 250 W. The glass substrate was then spin-coated with particle-free silver ink (EI-1207 from Electroninks) at 1000 rpm, followed by ramp-curing starting at 70 °C, with an increase of 10 °C every 15 minutes until a final curing temperature of 110 °C was reached. It took 30 minutes to completely cure the silver ink at this temperature. The silver was removed from the glass substrate using a razor blade, leaving it only in the trenches. To fully fill the trenches with silver, the process was repeated once more. Finally, the samples were sprayed with acetone, methanol, and IPA to remove any silver particulates, and PEDOT:PSS was spin-coated at 1500 rpm to achieve a thickness of 70 nm.

4.3. OLED Fabrication

The PEDOT:PSS layer was coated with thermally evaporated layers using shadow masks to complete the OLEDs, starting with 20 nm of 1,1-Bis[(di-4-tolylamino)phenyl]cyclohexane (TAPC) and 10 nm of 4,4',4"-Tris(carbazol-9-yl)triphenylamine (TCTA) as hole-transport layers, a 35 nm complex layer of TCTA and 1,3,5-Tri(p-pyrid-3-yl-phenyl)benzene (TpPyPB) doped with the green triplet emitter Tris(2-phenylpyridine)iridium(III) (Ir(ppy)3) in a 5:5:1 ratio, followed by a 25 nm electron-transport layer of TpPyPB. The cathode of the device consisted of a bilayer

Optics EXPRESS

of thermally evaporated LiF (1.2 nm) followed by aluminum (40 nm). Layers were deposited in an Angstrom EvoVac chamber at $<10^{-6}$ Torr and evaporated nominally at a rate of 1 Å per second (except for the green triplet emitter dopant which was evaporated at 0.2 Å per second. The devices of both ITO/glass and Ag-mesh were 10 mm^2, defined by the electrode overlap.

4.4. Metal mesh characterization

A probe station with a semiconductor device analyzer (B1500A Semiconductor Device Analyzer from Keysight Technologies) using four needle Van der Pau nonuniform method was used to measure sheet resistance. To get a high resolution image of the glass-embedded Ag micromesh, scanning electron microscopy (Zeiss SIGMA VP) was employed. The total and direct transmittance and reflectance were measured at the wavelength range of 400 to 800 nm using a UV-vis-NIR spectrometer with a 100 mm diameter integrating sphere (PerkinElmer Lambda 750). To measure roughness of the surface, an AFM (Bruker-Icon-VI) was used.

4.5. OLED characterization

The current density-voltage performances of the devices were measured using a Keithley model 2400 SourceMeter. At each voltage step a Hewlett Packard 4140B pA Meter/DC Voltage Source measured the photocurrent of a silicon photodiode to allow for luminance to be calculated. A homemade goniometer system is used to probe emission at various angles by rotating the photodiode probe at a fixed radius using a ThorLabs TDC001 servo controller. The emission spectrum was measured using a StellarNet EPP2000 spectrometer.

Funding. U.S. Department of Energy (DE-SC0018783).

Acknowledgments. The authors thank the Department of Energy for support under award DE-SC0018783.

Disclosures. The authors declare no conflicts of interest.

Data availability. Data underlying the results presented in this paper are not publicly available at this time but may be obtained from the authors upon reasonable request.

References

1. A. Salehi, Y. Chen, X. Fu, C. Peng, and F. So, "Manipulating Refractive Index in Organic Light-Emitting Diodes," ACS Appl. Mater. Interfaces **10**(11), 9595–9601 (2018). Publisher: American Chemical Society.
2. U. Shankar, D. Oberoi, and A. Bandyopadhyay, "A review on the alternative of indium tin oxide coated glass substrate in flexible and bendable organic optoelectronic device," Polym. Adv. Technol. **33**(10), 3078–3111 (2022).
3. X. Lu, Y. Zhang, and Z. Zheng, "Metal-Based Flexible Transparent Electrodes: Challenges and Recent Advances," Adv. Electron. Mater. **7**(5), 2001121 (2021).
4. W. Brütting, J. Frischeisen, T. D. Schmidt, B. J. Scholz, and C. Mayr, "Device efficiency of organic light-emitting diodes: Progress by improved light outcoupling: Device efficiency of OLEDs," Phys. Status Solidi A **210**(1), 44–65 (2013).
5. R.-P. Xu, Y.-Q. Li, and J.-X. Tang, "Recent advances in flexible organic light-emitting diodes," J. Mater. Chem. C **4**(39), 9116–9142 (2016). Publisher: The Royal Society of Chemistry.
6. T.-W. Koh, J. A. Spechler, K. M. Lee, C. B. Arnold, and B. P. Rand, "Enhanced Outcoupling in Organic Light-Emitting Diodes via a High-Index Contrast Scattering Layer," ACS Photonics **2**(9), 1366–1372 (2015).
7. J. Feng, Y.-F. Liu, Y.-G. Bi, and H.-B. Sun, "Light manipulation in organic light-emitting devices by integrating micro/nano patterns: Light manipulation in organic light-emitting devices by integrating micro/nano patterns," Laser Photonics Rev. **11**(2), 1600145 (2017).
8. "Bending Fatigue Study of Sputtered ITO on Flexible Substrate | IEEE Journals & Magazine | IEEE Xplore,".
9. R. Shinar and J. Shinar, "Light extraction from organic light emitting diodes (oleds)," J. Phys. Photonics **4**(3), 032002 (2022). Publisher: IOP Publishing.
10. Y. Qu, M. Slootsky, and S. R. Forrest, "Enhanced light extraction from organic light-emitting devices using a sub-anode grid," Nat. Photonics **9**(11), 758–763 (2015). Number: 11 Publisher: Nature Publishing Group.
11. K. Fehse, K. Walzer, K. Leo, W. Lövenich, and A. Elschner, "Highly Conductive Polymer Anodes as Replacements for Inorganic Materials in High-Efficiency Organic Light-Emitting Diodes," Adv. Mater. **19**(3), 441–444 (2007). _eprint: https://onlinelibrary.wiley.com/doi/pdf/10.1002/adma.200602156.
12. J. Choi, Y. S. Shim, C. H. Park, H. Hwang, J. H. Kwack, D. J. Lee, Y. W. Park, and B.-K. Ju, "Junction-free Electrospun Ag Fiber Electrodes for Flexible Organic Light-Emitting Diodes," Small **14**(7), 1702567 (2018). _eprint: https://onlinelibrary.wiley.com/doi/pdf/10.1002/smll.201702567.

Optics EXPRESS

13. D. S. Hecht, L. Hu, and G. Irvin, "Emerging transparent electrodes based on thin films of carbon nanotubes, graphene, and metallic nanostructures," Adv. Mater. **23**(13), 1482–1513 (2011).
14. J. Lee, T.-H. Han, M.-H. Park, D. Y. Jung, J. Seo, H.-K. Seo, H. Cho, E. Kim, J. Chung, S.-Y. Choi, T.-S. Kim, T.-W. Lee, and S. Yoo, "Synergetic electrode architecture for efficient graphene-based flexible organic light-emitting diodes," Nat. Commun. **7**(1), 11791 (2016). Number: 1 Publisher: Nature Publishing Group.
15. N. Li, S. Oida, G. S. Tulevski, S.-J. Han, J. B. Hannon, D. K. Sadana, and T.-C. Chen, "Efficient and bright organic light-emitting diodes on single-layer graphene electrodes," Nat. Commun. **4**(1), 2294 (2013). Number: 1 Publisher: Nature Publishing Group.
16. J. A. Spechler, T.-W. Koh, J. T. Herb, B. P. Rand, and C. B. Arnold, "A Transparent, Smooth, Thermally Robust, Conductive Polyimide for Flexible Electronics," Adv. Funct. Mater. **25**(48), 7428–7434 (2015). _eprint: https://onlinelibrary.wiley.com/doi/pdf/10.1002/adfm.201503342.
17. H.-Y. Xiang, Y.-Q. Li, S.-S. Meng, C.-S. Lee, L.-S. Chen, and J.-X. Tang, "Extremely Efficient Transparent Flexible Organic Light-Emitting Diodes with Nanostructured Composite Electrodes," Adv. Opt. Mater. **6**(21), 1800831 (2018).
18. L. Zhou, H.-Y. Xiang, S. Shen, Y.-Q. Li, J.-D. Chen, H.-J. Xie, I. A. Goldthorpe, L.-S. Chen, S.-T. Lee, and J.-X. Tang, "High-performance Flexible Organic Light-Emitting Diodes Using Embedded Silver Network Transparent Electrodes," ACS Nano **8**(12), 12796–12805 (2014). Publisher: American Chemical Society.
19. E. Jung, C. Kim, M. Kim, H. Chae, J. H. Cho, and S. M. Cho, "Roll-to-roll preparation of silver-nanowire transparent electrode and its application to large-area organic light-emitting diodes," Org. Electron. **41**, 190–197 (2017).
20. H. Cho, C. Yun, and S. Yoo, "Multilayer transparent electrode for organic light-emitting diodes: Tuning its optical characteristics," Opt. Express **18**(4), 3404–3414 (2010). Publisher: Optica Publishing Group.
21. Y.-W. Lim, O. E. Kwon, S.-M. Kang, H. Cho, J. Lee, Y.-S. Park, N. S. Cho, W.-Y. Jin, J. Lee, H. Lee, J.-W. Kang, S. Yoo, J. Moon, and B.-S. Bae, "Built-in Haze Glass-Fabric Reinforced Siloxane Hybrid Film for Efficient Organic Light-Emitting Diodes (oleds)," Adv. Funct. Mater. **28**(33), 1802944 (2018).
22. G. L. Ong, T. S. Ong, S. L. Yap, D.-J. Liaw, T. Y. Tou, S. S. Yap, and C. H. Nee, "A brief review of nanoparticles-doped PEDOT:PSS nanocomposite for OLED and OPV," Nanotechnol. Rev. **11**(1), 1870–1889 (2022). Publisher: De Gruyter.
23. M. Li, S. Sinha, S. Hannani, S. B. Walker, M. LeMieux, and P. W. Leu, "Ink-coated silver films on pet for flexible, high performance electromagnetic interference shielding and joule heating," ACS Applied Electronic Materials (2023).
24. M. Li, M. J. McCourt, A. J. Galante, and P. W. Leu, "Bayesian optimization of nanophotonic electromagnetic shielding with very high visible transparency," Opt. Express **30**(18), 33182–33194 (2022).
25. L. Meng, M. Zhang, H. Deng, B. Xu, H. Wang, Y. Wang, L. Jiang, and H. Liu, "Direct-writing Large-Area Cross-Aligned Ag Nanowires Network: Toward High-Performance Transparent Quantum Dot Light-Emitting Diodes," CCS Chem. **3**(8), 2194–2202 (2021). Publisher: Chinese Chemical Society.
26. K. M. Lee, R. Fardel, L. Zhao, C. B. Arnold, and B. P. Rand, "Enhanced outcoupling in flexible organic light-emitting diodes on scattering polyimide substrates," Org. Electron. **51**, 471–476 (2017).
27. Y. Zhang, J. Guo, D. Xu, Y. Sun, and F. Yan, "One-Pot Synthesis and Purification of Ultralong Silver Nanowires for Flexible Transparent Conductive Electrodes," ACS Appl. Mater. Interfaces **9**(30), 25465–25473 (2017).
28. T. Ye, L. Jun, L. Kun, W. Hu, C. Ping, D. Ya-Hui, C. Zheng, L. Yun-Fei, W. Hao-Ran, and D. Yu, "Inkjet-printed Ag grid combined with Ag nanowires to form a transparent hybrid electrode for organic electronics," Org. Electron. **41**, 179–185 (2017).
29. T. Gao and P. W. Leu, "The role of propagating modes in silver nanowire arrays for transparent electrodes," Opt. Express **21**(S3), A419 (2013).
30. H. Du, Y. Guo, D. Cui, S. Li, W. Wang, Y. Liu, Y. Yao, L. Zhao, and X. Dong, "Solution-processed PEDOT:PSS:GO/Ag NWs composite electrode for flexible organic light-emitting diodes," Spectrochim. Acta, Part A **248**, 119267 (2021).
31. J.-Y. Tseng, L. Lee, Y.-C. Huang, J.-H. Chang, T.-Y. Su, Y.-C. Shih, H.-W. Lin, and Y.-L. Chueh, "Pressure Welding of Silver Nanowires Networks at Room Temperature as Transparent Electrodes for Efficient Organic Light-Emitting Diodes," Small **14**(38), 1800541 (2018). _eprint: https://onlinelibrary.wiley.com/doi/pdf/10.1002/smll.201800541.
32. Y.-s. Liu, J. Feng, X.-L. Ou, H.-f. Cui, M. Xu, and H.-B. Sun, "Ultrasmooth, highly conductive and transparent PEDOT:PSS/silver nanowire composite electrode for flexible organic light-emitting devices," Org. Electron. **31**, 247–252 (2016).
33. Z. Zhou, S. B. Walker, M. LeMieux, and P. W. Leu, "Polymer-embedded Silver Microgrids by Particle-Free Reactive Inks for Flexible High-Performance Transparent Conducting Electrodes," ACS Appl. Electron. Mater. **3**(5), 2079–2086 (2021). Publisher: American Chemical Society.
34. H. B. Lee, W.-Y. Jin, M. M. Ovhal, N. Kumar, and J.-W. Kang, "Flexible transparent conducting electrodes based on metal meshes for organic optoelectronic device applications: a review," J. Mater. Chem. C **7**(5), 1087–1110 (2019).
35. F. L. M. Sam, M. A. Razali, K. I. Jayawardena, C. A. Mills, L. J. Rozanski, M. J. Beliatis, and S. R. P. Silva, "Silver grid transparent conducting electrodes for organic light emitting diodes," Org. Electron. **15**(12), 3492–3500 (2014). Publisher: Elsevier.
36. T. Gao, B. Wang, B. Ding, J.-k. Lee, and P. W. Leu, "Correction to Uniform and Ordered Copper Nanomeshes by Microsphere Lithography for Transparent Electrodes," Nano Lett. **14**(6), 3694 (2014).
37. T. Gao, Z. Li, P.-S. Huang, G. J. Shenoy, D. Parobek, S. Tan, J.-K. Lee, H. Liu, and P. W. Leu, "Hierarchical graphene/metal grid structures for stable, flexible transparent conductors," ACS Nano **9**(5), 5440–5446 (2015).

Optics EXPRESS

38. T. Gao, P.-S. Huang, J.-K. Lee, and P. W. Leu, "Hierarchical metal nanomesh/microgrid structures for ordered and uniform transparent electrodes," RSC Adv. **5**(87), 70713–70717 (2015).
39. T. Kamijo, S. de Winter, P. Panditha, and E. Meulenkamp, "Printed Copper Grid Transparent Conducting Electrodes for Organic Light-Emitting Diodes," ACS Appl. Electron. Mater. **4**(2), 698–706 (2022). Publisher: American Chemical Society.
40. L. Yao, Y. Qin, X. Li, Q. Xue, F. Liu, T. Cheng, G. Li, X. Zhang, and W. Lai, "High-efficiency stretchable organic light-emitting diodes based on ultra-flexible printed embedded metal composite electrodes," InfoMat **5**(5), e12410 (2023).
41. T. Gao and P. W. Leu, "Copper nanowire arrays for transparent electrodes," J. Appl. Phys. **114**(6), 063107 (2013).
42. M. Li, M. Zarei, K. Mohammadi, S. B. Walker, M. LeMieux, and P. W. Leu, "Silver Meshes for Record-Performance Transparent Electromagnetic Interference Shielding," ACS Appl. Mater. Interfaces p. acsami.3c02088 (2023).
43. C. Peng, C. Chen, K. Guo, Z. Tian, W. Zhu, T. Xu, and B. Wei, "Organic light-emitting diodes using novel embedded al gird transparent electrodes," Phys. E **87**, 118–122 (2017).
44. S.-R. Shin, H. B. Lee, W.-Y. Jin, K.-J. Ko, S. Park, S. Yoo, and J.-W. Kang, "Improving light extraction of flexible OLEDs using a mechanically robust Ag mesh/ITO composite electrode and microlens array," J. Mater. Chem. C **6**(20), 5444–5452 (2018).
45. S. Park, J. T. Lim, W.-Y. Jin, H. Lee, B.-H. Kwon, N. S. Cho, J.-H. Han, J.-W. Kang, S. Yoo, and J.-I. Lee, "Efficient Large-Area Transparent OLEDs Based on a Laminated Top Electrode with an Embedded Auxiliary Mesh," ACS Photonics **4**(5), 1114–1122 (2017).
46. J. H. Park, D. Y. Lee, Y.-H. Kim, J. K. Kim, J. H. Lee, J. H. Park, T.-W. Lee, and J. H. Cho, "Flexible and Transparent Metallic Grid Electrodes Prepared by Evaporative Assembly," ACS Appl. Mater. Interfaces **6**(15), 12380–12387 (2014).
47. W. Zhou, J. Chen, Y. Li, D. Wang, J. Chen, X. Feng, Z. Huang, R. Liu, X. Lin, H. Zhang, B. Mi, and Y. Ma, "Copper Mesh Templated by Breath-Figure Polymer Films as Flexible Transparent Electrodes for Organic Photovoltaic Devices," ACS Appl. Mater. Interfaces **8**(17), 11122–11127 (2016).
48. M.-G. Kang and L. J. Guo, "Nanoimprinted semitransparent metal electrodes and their application in organic light-emitting diodes," Adv. Mater. **19**(10), 1391–1396 (2007).
49. Y. Wang, Y. Liu, T. Wang, S. Liu, Z. Chen, and S. Duan, "Low-temperature nanowelding silver nanowire hybrid flexible transparent conductive film for green light OLED devices," Nanotechnology **33**(45), 455201 (2022).
50. A. J. Galante, M. Li, B. Pilsbury, M. LeMieux, Q. Liu, and P. W. Leu, "Achieving highly conductive, stretchable, and washable fabric from reactive silver ink and increased interfacial adhesion," ACS Applied Polymer Materials (2022).
51. M. Li, M. Zarei, K. Mohammadi, and P. W. Leu, "Silver meshes for record-performance transparent electromagnetic interference shielding," ACS Appl. Mater. Interfaces (2023).
52. M. Li, M. Zarei, A. J. Galante, B. Pilsbury, S. B. Walker, M. LeMieux, and P. W. Leu, "Stretchable and wash durable reactive silver ink coatings for electromagnetic interference shielding, joule heating, and strain sensing textiles," Prog. Org. Coat. **179**, 107506 (2023).
53. S. Haghanifar, T. Gao, R. T. R. D. Vecchis, B. Pafchek, T. D. B. Jacobs, and P. W. Leu, "Ultrahigh-transparency, ultrahigh-haze nanograss glass with fluid-induced switchable haze," Optica **4**(12), 1522–1525 (2017).
54. S. Haghanifar, P. Lu, M. Imrul Kayes, S. Tan, K.-J. Kim, T. Gao, P. Ohodnicki, and P. W. Leu, "Self-cleaning, high transmission, near unity haze OTS/silica nanostructured glass," J. Mater. Chem. C **6**(34), 9191–9199 (2018).
55. S. Haghanifar, A. J. Galante, M. Zarei, J. Chen, S. Tan, and P. W. Leu, "Mechanically durable, super-repellent 3D printed microcell/nanoparticle surfaces," Nano Res. **15**(6), 5678–5686 (2022).
56. S. B. Walker and J. A. Lewis, "Reactive silver inks for patterning high-conductivity features at mild temperatures," J. Am. Chem. Soc. **134**(3), 1419–1421 (2012). PMID: 22220580.